PCCP

In situ electrochemical Raman investigation of charge storage in rGO and N-doped rGO

Journal:	*Physical Chemistry Chemical Physics*
Manuscript ID	CP-ART-01-2021-000248.R1
Article Type:	Paper
Date Submitted by the Author:	05-Apr-2021
Complete List of Authors:	Yadav, Rohit; Toyota Technological Institute, Graduate School of Engineering Joshi, Prerna; Toyota Technological Institute, Graduate School of Engineering Hara, Masanori; Toyota Technological Institute Yoshimura, Masamichi; Toyota Technological Institute

ARTICLE

In situ electrochemical Raman investigation of charge storage in rGO and N-doped rGO

Received 00th January 20xx,
Accepted 00th January 20xx

DOI: 10.1039/x0xx00000x

Rohit Yadav,* Prerna Joshi, Masanori Hara, and Masamichi Yoshimura

In this study, *in situ* electrochemical Raman spectroscopy was applied to clarify the charge storage mechanism in three types of anodes, synthetic graphite, reduced graphene oxide (rGO), and nitrogen-doped reduced graphene oxide (N-rGO). Li^+ intercalation phenomenon was measured in $LiPF_6$ electrolyte solution using a modified coin cell setup. The synthetic graphite anode showed the splitting of G peak at E< 0.2 V vs Li/Li^+, corresponding to the formation of graphite intercalation compound (GIC) and its second-order 2D peak was found red-shifted due to charge transfer and induced strain in the potential region of 0.5 to 0.15 V vs Li/Li^+. In the case of rGO, the lattice defects assisted in large and early intercalation of electrolyte ions, which is confirmed by the red-shift in G peak (~36 cm^{-1}) and its early disappearance below 0.3 V vs Li/Li^+, respectively. Unlike rGO, nitrogen vacancies in N-rGO provide active sites for Li^+ intercalation, resulting in enhanced charge transfer, displayed by large red-shift in G peak (~55 cm^{-1}) and blue-shift in the D peak. In addition, a new Raman peak at 1850 cm^{-1} was observed in N-rGO for the first time, corresponding to the formation of a reversible intermediate species from the interaction between Li^+ and nitrogen vacancies. This work demonstrates the use of a simple *in situ* technique to get insight into the nano-carbon electrodes during device operation and to reveal the role of doped nitrogen atoms for Li^+ intercalation.

Introduction

Because of their interesting mechanical, electrical, and structural properties, carbon materials are of great interest for more than two decades for applications in energy devices such as batteries,[1] supercapacitors,[2] and fuel cells.[3,4] Utilizing the aforementioned features, carbonaceous materials such as graphite, pristine graphene, and chemically modified graphene have already been explored as energy storage materials,[2] and further researches are going on to tailor their chemical and structural properties, namely defective sites, functionalities, heteroatom doping, and surface area.[5,6] The primary task of improving the performance is not only limited to the discovery of new material but also depends on the detailed investigation of electrode behaviors during device operation. It is vital to acquire real-time insight into the charge storage mechanism and physiochemical change occurring at the electrode-electrolyte interfaces such as structure growth, ion intercalation mechanism, interface formation, electrode degradation, and phase change. In this regard, *in situ* or *in operando* analytical techniques pave a path to study these electrode phenomena in a dynamic system.[7–10] Raman spectroscopy is one of such sensitive, non-destructive, and well-developed technique to study structural properties in carbon materials by the appearance of a first-order G peak, a second-order 2D Raman peak, and a defect induced D peak. G and D peaks arise from the double degenerate (E_{2g}) vibration mode of in-plane sp^2 C-C bond and breathing mode of defective sp^3 carbon ring, respectively, while the 2D peak is the second overtone of D peak which arises from the inelastic scattering event involving two phonons of opposite wave vectors.[11,12] The 2D peak includes important information such as induced strain, charge transfer, external doping, and the number of layers. The versatile and well-explored nature of Raman spectroscopy makes it the first choice to be combined with electrochemical measurements for carbon-based electrodes.

Inaba *et al.* first studied the *in situ* electrochemical (EC) Raman spectroscopy for Li-ion battery using a highly oriented pyrolytic graphite (HOPG) electrode.[13] The work was a breakthrough because it was the first report that showed the graphite intercalation compound (GIC) formation in the HOPG anode and correlated it with the G peak splitting. Till now, various other carbon electrode materials such as microcrystalline KS-44 graphite,[14,15] pristine graphene,[16] and activated carbon,[15,17] have been investigated by *in situ* EC Raman spectroscopy for application in supercapacitor and lithium-ion batteries. Most of the studied carbon forms are either crystalline graphite or few-layered graphene. However, the charge storage mechanisms in defective graphene created by oxygen functionalities, heteroatom doping,[18] or structural defect have not been focused on so far. Previous researches to improve the electrode performance have reported that defective and chemically derived electrode material such as reduced graphene oxide (rGO) and nitrogen-doped reduced

Graduate School of Engineering, Toyota Technological Institute, Nagoya 468-8511, Japan. E-mail: sd19503@toyota-ti.ac.jp

Electronic Supplementary Information (ESI) available: Fig. S1-S9, showing XRD of graphite, rGO, and N-rGO; XPS N1s deconvolution of N-rGO; TEM of graphite, rGO, and N-rGO and SAED of graphite; charge profile of graphite, rGO, and N-rGO; *in situ* Raman of de-intercalation in N-rGO; *in situ* Raman of N-rGO synthesized at 600, 700, and 900 °C; cyclic stability of rGO and N-rGO; XPS of charged rGO and N-rGO; table S1 and S2. See DOI: 10.1039/x0xx00000x

graphene oxide (N-rGO) show higher capacity ~600-1500 mAh g^{-1},[19–21] than the theoretical capacity of graphite (372 mAh g^{-1}).[22] This is because the defect structure and functionalities affect the chemistry of Li-ion intercalation.

The present study emphasizes on the behavior of these defective carbon as a Li-battery anode and reflects structural changes occurring in the system during operating conditions, highlighting the limitation of *ex situ* measurements. These changes can provide an insight related to the charge transfer, developed strain, and intermediate formation[23] in the electrode using a feasible, cost-effective, and highly sensitive technique of *in situ* EC Raman spectroscopy. In this study, using *in situ* EC Raman spectroscopy, we have observed red and blue-shifts in G and D peaks respectively, which are associated with enhanced charge transfer and accumulation of Li-ions at defectives sites in rGO and N-rGO electrodes. Specifically, an additional new reversible Raman peak at 1850 cm^{-1} appeared for N-rGO, which could be due to the formation of an intermediate species by the interaction between Li^+ and N vacancies. Also, the behavior of the second-order peak (2D) is only limited to highly crystalline graphite anodes,[16,24,25] thus, an effort has been made to investigate it for synthetic graphite anode. This is the first *in situ* report on the Li-intercalation mechanism in rGO and N-rGO.

Experimental

Electrode preparation:

Briefly, rGO and N-rGO were synthesized from graphene oxide (GO) prepared by modified Hummers' method via pyrolysis at 800 °C in the absence and presence of urea, respectively, as described in our previously reported article.[2] The electrode slurry was prepared by mixing with 5 wt.% of polyvinylidene fluoride (PVDF, Alfa Aesar) as binder in N-methyl-2-pyrrolidone (NMP, Aldrich) solvent. The slurry was drop casted on a cleaned (ultrasonicated in ethanol for 30 min) stainless steel wire mesh (SUS 304, diameter 14 mm, Nilaco Corporation). The slurry coated mesh electrode was dried in vacuum at 80 °C for 8 h. For comparison, a synthetic graphite electrode (average particle size< 21 µm, Aldrich) was also prepared in a similar manner.

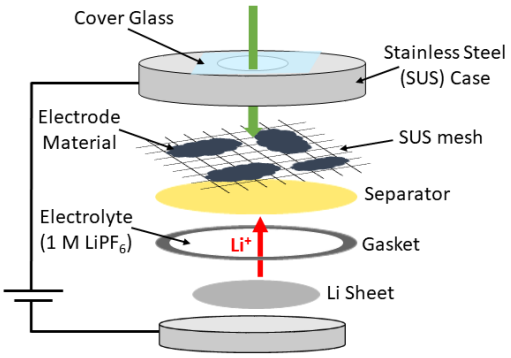

Fig. 1 Schematic of the customized coin cell setup.

Coin cell setup:

All *in situ* measurements were performed in a customized 2032-coin cell setup with a hole of 0.2 mm in diameter on the top of the cell, as shown in fig. 1. The coin cell was fabricated in an Ar filled (99.99 % pure) glove box (UNICO Ltd.), with electrode material deposited SUS mesh as a working electrode, Li metal (99.9 % pure, Honjo Metal Co., Ltd.) as counter and reference electrode, and Whatman® GF/A microfiber filter paper as a separator in 1 M lithium hexafluorophosphate ($LiPF_6$) containing electrolyte in solution ethylene carbonate (EC): dimethyl carbonate (DMC) = 1:1 v/v %. The coin cell assembly was crimped and the top hole was sealed with cover glass using epoxy paste (Torr seal®) inside the glove box. The cover glass was fixed carefully to avoid the exposure of cell contents to air or epoxy paste. The sealed cell was kept for 2 h inside the glove box for the epoxy to settle and dry.

***In situ* electrochemical Raman measurement:**

Raman measurements were performed by in-Via Renishaw Raman spectroscope using 532 nm laser focused by 50x long objective lens. All the measurements were performed in static mode with 0.5 % laser power (to avoid laser-induced defects) and 1.5 s exposure time for 5 accumulations to obtain a high signal to noise ratio. The *in situ* cell was studied by galvanostatic charge-discharge (without resting time), cycled at C-rate= C/15 (1C= charge required to fully intercalate Li^+ into graphite anode, forming LiC_6 in 1 h) in the potential range from 10 mV to 3 V using the potentiostat (Hokuto Denko HZ-7000). Prior to measurement, the open-circuit potential (OCP) of the sealed cell was monitored till it became stable. All the potentials are represented w.r.t Li/Li^+ unless otherwise stated.

Material characterizations:

X-ray diffraction (XRD) was performed by Cu K_α (λ= 1.5405 Å) radiation source using Rigaku Ultima IV X-ray diffractometer, to study the reduction and interlayer *d* spacing. N-doping and surface functionalities were investigated by X-ray photoelectron spectroscopy (XPS) using a monochromatic Al K_α X-ray source (ULVAC-PHI 5000 VersaProbe-II). The surface morphology and crystallinity of the samples were studied by transmission electron microscopy (TEM) (JEOL JEM-2100), operated at 120 kV.

Results and Discussion

The successful reduction of GO to rGO and N-rGO was confirmed by XRD (fig. S1). The calculated *d* spacing corresponding to the (002) plane for synthetic graphite was *d*= 0.33 nm, and that both for rGO and N-rGO was 0.34 nm. This slightly high *d* value for rGO and N-rGO is due to remaining oxygen functional groups after reduction.[26] The degree of reduction and nitrogen incorporation in N-rGO were further confirmed by XPS, as shown in fig. 2(a). XPS survey scan shows the presence of C, O, and N elements without any impurities with N-doping of 8.7 at. % in N-rGO. The calculated C/O ratio for rGO and N-rGO was 14.8 and 23.0 respectively, confirming the successful synthesis from the reduction of GO. Fig. S2 shows the individual N1s scan of the synthesized N-rGO sample, which

allows a better understanding of N incorporation in the graphene framework. Four types of N functionalities, pyridinic nitrogen (N-6), pyrrolic nitrogen (N-5), graphitic nitrogen (N-G), and nitrogen oxide (N-O) can be deconvoluted from N1s spectrum, present in the concentration of 23.6, 22.3, 45.2, and 8.8 %, respectively. N-6 is formed due to the replacement of the C atom at the edge of the graphene and is bonded to 2 sp^2 C atoms. The substitution of C by N in a 5-member ring leads to the formation of N-5 which has more sp^3 character. The substitution of C by N in between the lattice forms N-G which bonds to 3 sp^2 C atoms.[27,28] N-6 and N-5 functionalities are reported to induce metallic behavior and electron donor state near Fermi level,[29,30] while N-G provides catalytically active sites, which overall enhances the interaction between Li^+ and N-vacancies compared to the un-doped graphene (rGO).[31,32] TEM micrographs in fig. S3(a) show the stacked and wrinkle-free flakes of graphite, whereas exfoliated and wrinkled morphology in the case of rGO and N-rGO (fig. S3 (b) and (c)) due to pyrolysis. Selected area electron diffraction (SAED) micrographs in fig. S3(d) shows the polycrystalline nature of the synthetic graphite anode with a ring diameter ~9.5 nm^{-1}. The Raman spectra of graphite, rGO, and N-rGO are shown in fig. 2(b). Sharp G (~1576 cm^{-1}) and 2D (~2711 cm^{-1}) peaks are observed in the case of synthetic graphite due to its ordered stacked structure. A small intensity D peak is also observed at ~1350 cm^{-1}. On the other hand, two broad D (~1350 cm^{-1}) and G (~1590 cm^{-1}) peaks were observed due to structural defects for rGO, and structural and nitrogen-induced defects for N-rGO at high pyrolysis temperatures. The ratio of the intensity of D and G peak (I_D/I_G) was used to investigate the degree of defects in the graphene lattice. The calculated I_D/I_G ratio for rGO and N-rGO samples was 0.94 ± 0.02 and 1.14 ± 0.02, respectively. The ratio of the intensity of D and G peak (I_D/I_G) was used to investigate the degree of defects in the graphene lattice. The calculated I_D/I_G ratios for rGO and N-rGO samples were 0.94 ± 0.02 and 1.14 ± 0.02, respectively. The large I_D/I_G ratio of N-rGO compared to rGO is due to nitrogen incorporation, which creates nitrogen-induced defects in the lattice[27,33] and due to extra synthesis step in the case of N-rGO like freeze-drying and washing in HCl solution.[2]

Fig. 3 shows the cyclic voltammogram (CV) of the first cycle to compare lithium-ion intercalation/de-intercalation behavior in graphite, rGO, and N-rGO at a scan rate of 0.1 mV s^{-1}. During intercalation, a cathodically polarized peak at E< 0.8 V is observed for graphite anode and is ascribed to solid electrolyte interface (SEI) formation by the decomposition of the electrolyte and electrode materials.[34,35] In general, SEI formation occurs during the first intercalation cycle by the reduction of electrolyte components at the electrode surface, which makes first cycle important for *in situ* investigation. On reducing the potential, another well-defined and reversible CV peak in the potential range ~0.20 to 0.02 V was observed due to reversible intercalation and de-intercalation of Li^+ ions into the graphite layers through the formation of graphite intercalation compounds (GIC). A small shoulder peak to the main peak can be observed in the potential range ~0.1V, signifying the transition from stage 2 (partial intercalation of Li-ions in graphite layers) to stage 1 GIC, i.e. the formation of the final intercalation compound where all graphite layers are filled with intercalated Li-ions.[16] In the case of rGO and N-rGO, various cathodic peaks are present below 1.5 V, corresponding to the decomposition of electrolyte and the reduction of attached oxygen functional groups on the electrode surface contributing to the formation of SEI. The cathodic peak positions for rGO and N-rGO are at a higher positive potential than graphite, which could be due to the early intercalation of Li^+ into their defective structure as compared to the layered graphitic structure. Additionally, an early increase of specific current in CV profile for rGO/N-rGO is also observed, which can also be due to the above-mentioned reason. At lower potential (E< 0.5 V), an irreversible Li^+ insertion peak was observed in both rGO and N-rGO, which pointed towards the irreversible Li^+ intercalation/de-intercalation mechanism.[19,36,37]

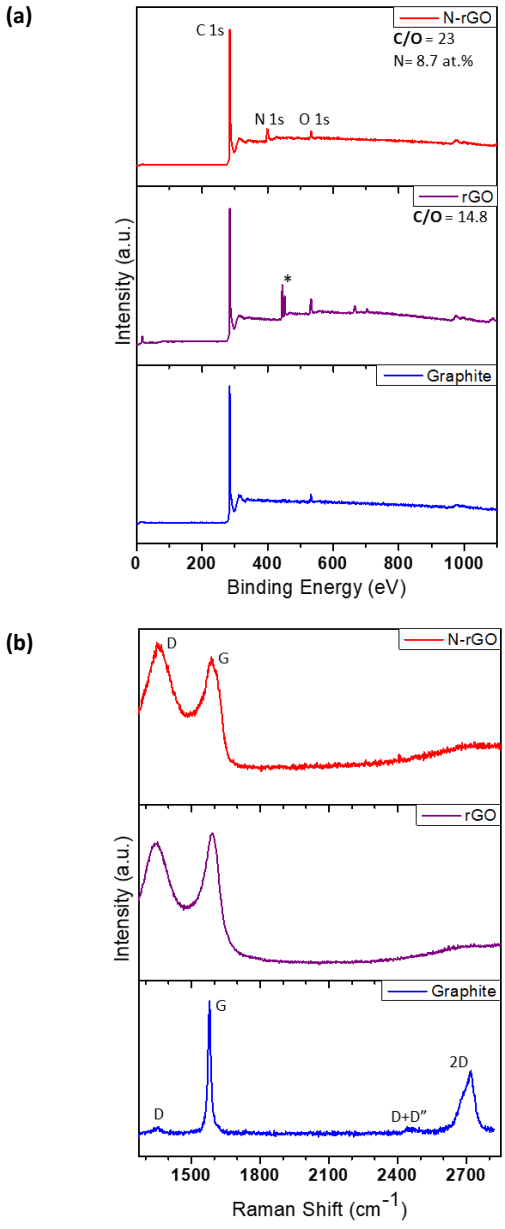

Fig. 2 Comparison of (a) XPS and (b) Raman spectra of synthetic graphite, rGO, and N rGO (* refer to the Indium substrate).

No additional reversible peaks are present for both rGO and N-rGO, signifying that the GIC formation in both electrodes is unlikely.[15,17] Electrochemical measurement solely cannot provide mechanistic details supporting the above arguments regarding the reaction mechanism, early Li^+ intercalation, and Li^+-nitrogen interaction for rGO/N-rGO electrodes, thus *in situ* Raman spectroscopy is employed to precisely investigate these arguments. The *in situ* EC Raman measurement was performed during the first galvanostatic charge-discharge cycle at a C-rate= C/15. The low C-rate was chosen for the precise investigation of Raman spectra changes occurring on the electrode surface. The first cycle capacity of graphite, rGO, and N-rGO was 282, 630, 800 mA h g^{-1}, as shown in fig. S4. The lower observed capacity of graphite than theoretical capacity (372 mA h g^{-1}) is due to the non-uniform coating of the electrode material on the SUS mesh and non-inclusion of acetylene black, which is used to overcome the conductivity loss by PVDF binder.[38]

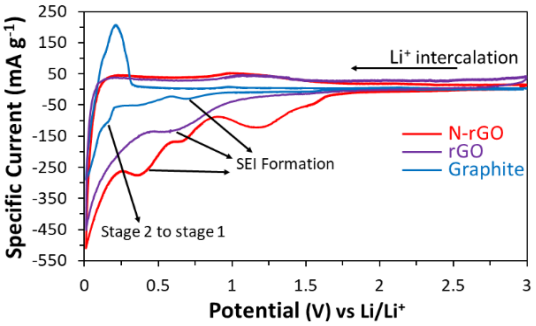

Fig. 3 Cyclic voltammetry profile of synthetic graphite, rGO, and N-rGO at 0.1 mV s^{-1} from modified coin cell setup.

Synthetic graphite:

The working of the modified coin cell setup was confirmed by the G peak splitting, which was reported in previous studies[15,16,25] in *in situ* EC Raman spectroscopy of the synthetic graphite electrode. As shown in fig. 4 (a), two main Raman peaks i.e. G (~1582 cm^{-1}) and 2D (~2724 cm^{-1}) peaks were observed at OCP (3.0 V). The peak position and intensity changed soon after cell fabrication, probably due to the developed pressure or deformity in the anode.[39] During the first intercalation cycle, Raman peaks remain fairly unchanged until 0.5 V, showing that no structural change of graphite takes place in this potential region, whereas a small peak was observed on the CV. Below 0.5 V, significant reversible changes were observed in the Raman spectra; (a) the blue-shift in G peak, (b) gradual weakening and red-shift in 2D peak, (c) splitting of G peak below 0.2V, and (d) the gradual disappearance of all Raman peaks below 0.09 V.

The G peak shifted from *ca.* 1580 to 1591 cm^{-1} in the potential range 0.50 to 0.20 V (indicated by the blue arrow in fig. 4 and summarized in table S1) due to the formation of an initial stage of Li^+ intercalation (dilute stages GIC), which resulted in the increased force constant of the in-plane sp^2 C-C bond in the periodically arranged graphite lattice, as reported by Sole *et al.*[24] and Inaba *et al.*[13]. The further intercalation of Li^+ into graphite via staged GIC (stage 4 to stage 1) was first explained in the pioneering work of Inaba *et al.* from the splitting of G peak in the highly oriented pyrolytic graphite. At potential E< 0.2 V, the G peak is splitted into two peaks E_{2g2}(i)= 1573 cm^{-1} and E_{2g2}(b)= 1600 cm^{-1}, E_{2g2}(i) is the interior graphite layers, which are not adjacent to the intercalated Li^+ and E_{2g2}(b) is the bounding graphite layer, adjacent to the intercalated Li^+.[25,40] As E≤ 0.1 V, E_{2g2}(i) peak completely vanishes and only the E_{2g2}(b) peak remains, showing the complete intercalation of the anode by Li^+ and the formation of stage 2 GIC. In further lower potential region E≤ 0.08 V, the electrical conductivity of the anode increases due to the formation of final stage GIC (stage 1). Due to the formation of high conducting GIC, the polarizability of graphite anode changes which decreases the optical skin depth of the Raman laser and the Raman scattering intensity gradually diminishes, leading to the disappearance of Raman peaks.[24]

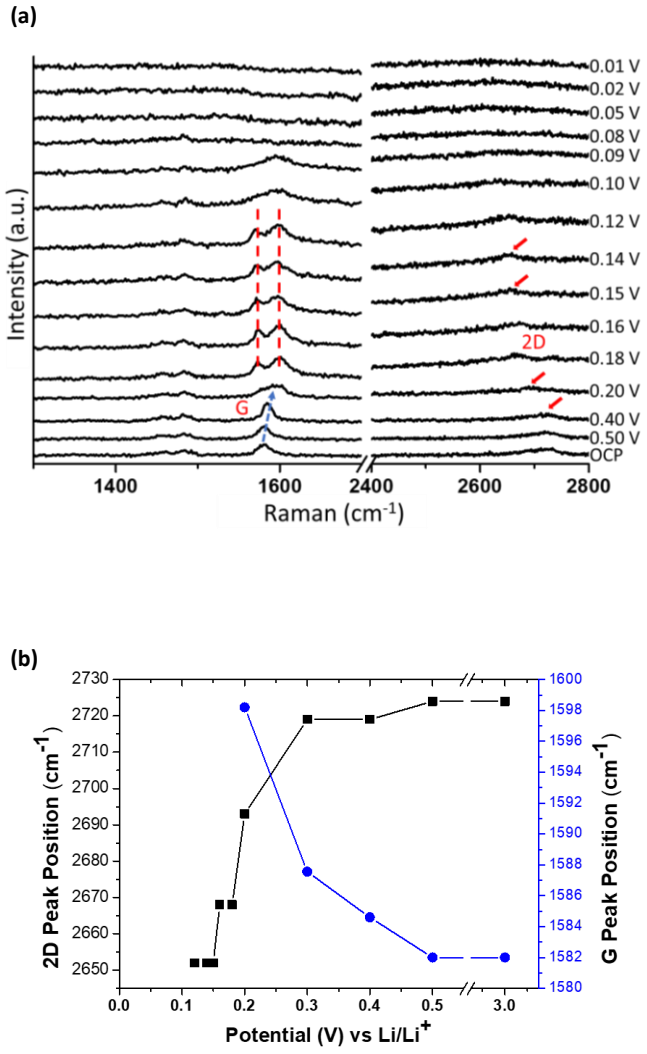

Fig. 4 (a) *In situ* EC Raman spectra of Li^+ intercalation into synthetic graphite, (b) Corresponding change in Raman G and 2D peak of synthetic graphite during first intercalation cycle.

The behavior of the 2D peak during intercalation has not yet been reported for synthetic graphite anodes. The position of double resonance 2D peak (~2724 cm^{-1}) remained unchanged until 0.5 V, and red-shifted from *ca.* 2724 to 2719 cm^{-1} between 0.5 to 0.3 V. Then, the peak further weakened and red-shifted to 2652 cm^{-1} at 0.15 V (Δ2D= 72±1 cm^{-1}) until it disappeared completely at E< 0.12 V, as shown in fig. 4 (b). The 2D Raman peak is reported to be influenced by layer stacking, charging, and induced strain in graphene.[11,12] The observed red-shift in our case could also arise due to the charging of graphite, i.e. the formation of highly conductive final stage GIC[41] and the developed deformational strain from Li^+ intercalation.[42] The charging of graphite occurs because of the intercalation of Li^+ between the layered graphite structure. The intercalation occurs via a staging mechanism, i.e. in the initial stage (stage 4), one Li^+ ion is shared between 72 C atoms forming LiC_{72} compound, which continues to the final stage (stage 1) where one Li^+ is shared among 6 C atoms forming LiC_6.[43] Therefore, as the intercalation proceeds from LiC_{72} to LiC_6, more Li^+ intercalate between the graphite layers leading to the enhanced charge transfer since one intercalated Li-ion transfers 0.08|e| charge to the pristine graphene (without defects), as calculated theoretically by Ma *et al*.[30] The intercalation of Li^+ can further deform graphite structure in terms of stretching/expansion of in-plane C-C bond, which can create uniaxial[44] or biaxial[42] lattice strain in the graphite structure. The strain also originates from the increased electron density and possible steric hindrance due to intercalated ions.[16] The widely invoked Daumas–Hérold model on intercalation phenomena postulates the deformity of graphene layer around intercalant.[24] Chacon-Torres *et al.* and Sole *et al.* observed a similar red-shift (77 cm^{-1}) and simultaneous weakening of the 2D peak for a crystalline graphite anode. It would be interesting to note that the shift is similar in our case, although synthetic graphite is less crystalline than reported highly crystalline graphite.[24,42]

Reduced graphene oxide (rGO):

As shown in fig. 5, only two dominated Raman peaks, D (~1342 cm^{-1}) and G (~1591 cm^{-1}) were observed at OCP (2.9 V) in the case of rGO and their intensity ratio, I_D/I_G is 1.08. CV profile of rGO/N-rGO show various cathodic peaks below 1.5 V corresponding to the SEI formation however, the absence of any additional peak in Raman spectra shows that the formed SEI is Raman inactive. During the negative sweep, the position of the D peak remained fairly intact and no splitting of G peak was observed, which confirms that the formation of staged GIC is unlikely in the case of defective structures like rGO and N-rGO, as was also claimed from the above CV analysis. Although one may think that the formation of a staged GIC can occur from the remaining ordered stacking of rGO, the G peak is broad enough (FWHM~ 75 cm^{-1}) to suppress any observable peak splitting.[16,45]

Further, during the negative sweep, G peak remained almost unchanged until 1.8 V (1591 cm^{-1}), and then red-shifted to 1555 cm^{-1} until 0.35 V. The total red-shift in the G peak from OCP to 0.35 V was *ca.* 36 cm^{-1}. The G peak shift can be attributed to the charge transfer to the rGO lattice.[46] The negative charge transfer to the rGO lattice from the controlled potential sweep during the anodic scan leads to the accumulation of counter ions (Li^+). This negative charge transfer results in the occupation of antibonding states (π^*), leading to the elongation and subsequent weakening of the C-C bond length in rGO.[47,48] Weakening of the C-C bond prompts the red-shit of the Raman G peak. Similar behavior for the G peak was also observed for disordered carbon electrodes such as activated carbon,[15] polyparaphenylene-based disordered carbon,[49] low-temperature pyrolytic carbon,[50] and mesocarbon microbeads.[51] Along with the red-shift, the weakening of individual D and G Raman peak was observed until it completely disappeared at potential below 0.30 V. This could also be due to the same reason as explained in the case of graphite anode. It is noted that the complete disappearance of Raman peaks in the case of rGO occurred at a significantly higher potential region (E< 0.30 V) than graphite (E< 0.08 V). The structural defects and exfoliated rGO sheets facilitate complete intercalation of Li^+ at higher potential and hence, the electrical conductivity of rGO increased earlier than graphite leading to the early disappearance of Raman intensity. The Raman spectra change in rGO supports the above argument from CV profile (fig. 3), where the high potential cathodic peaks and early increase of specific current were observed for rGO and N-rGO as compared to graphite. The large accumulation and coverage of rGO lattice by Li^+ will also contribute to the decrease in Raman intensity from sp^2 C-C bond vibration.[19]

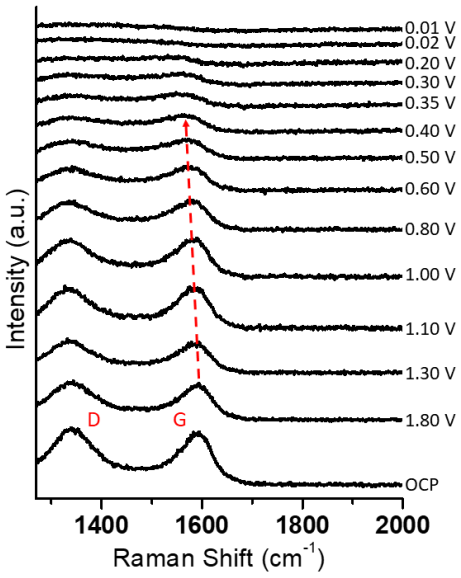

Fig. 5 *In situ* EC Raman spectra of Li^+ intercalation into rGO anode.

Nitrogen-doped reduced graphene oxide (N-rGO):

As shown in fig. 6(a) and 6(b), G peak was positioned around 1593 cm^{-1} at OCP (2.7 V) which fluctuated slightly until 0.7 V and

then decreased/red-shifted to 1538 cm^{-1} with the decrease in potential to 0.30 V. The total G peak shift for N-rGO was *ca.* 55 cm^{-1} as compared to the 36 cm^{-1} for rGO. Since this red-shift is associated with charge transfer, a large red-shift implies that the amount of charge transferred to N-rGO electrode is larger than that on rGO electrode. Besides, the D peak position was also observed to be blue-shifted from 1350 cm^{-1} at OCP to 1357 cm^{-1} at 0.5 V (*ca.* $\Delta D = 7$ cm^{-1}), while in the case of rGO electrode, it remained unchanged (fig. 5). Based on the large charge transfer argument along with the shift in D peak position, the following description about charge storage in N-rGO can be considered. It is reported theoretically that various types of nitrogen vacancies work as active sites for electrolyte ions because of the high electronegativity of nitrogen than carbon and hybridization of π electrons with the nitrogen lone pair.[30,31] As a result, more number of Li^+ tends to accumulate at these N-vacancies compared to lattice defects, like in rGO, created from high pyrolysis temperature. A significant accumulation of Li^+ at N-vacancies is expected to result in a greater charge transfer to the N-rGO electrode, which induces a larger red-shift in the G peak as compared to the rGO electrode. Additionally, the presence of Li^+ at N-vacancies can hinder the breathing mode of the carbon ring, as a consequence, a blue-shift is observed in the Raman D peak.[14] Ma *et al.* used a grid-based Bader analysis algorithm, to compare the amount of charge transfer from intercalated Li^+ to the N-doped and undoped graphene lattice. It was observed that more charge is transferred in the case of N-doped graphene (0.84|e|) as compare to un-doped graphene (0.70|e|), which supports our description.[30] As the potential is further decreased, both D and G peak intensities weakened and disappeared eventually (E< 0.3 V), as was observed in the case of rGO.

At further lower potential (E< 0.05 V), a new and only Raman peak appeared at *ca.* 1850 cm^{-1}. This type of peak is not reported and not characteristic of graphene-based electrodes. This Raman peak is reversible and disappeared with the application of positive potential, shown in fig. S5. Conventional electrochemical measurements failed to observe any indication of this new Raman peak, although is observed clearly in the *in situ* Raman analysis, highlighting the advantages of *in situ* measurements. To confirm the reproducibility and origin of this peak, we also tested three other N-rGO samples, prepared at different pyrolysis temperatures i.e. 600, 700, and 900 °C. As reported in our previous report,[2] the pyrolysis temperature affects the extent of nitrogen doping, nitrogen functionalities, degree of reduction, etc. It is interesting to note that the N-rGO samples synthesized at pyrolysis temperatures 700 and 900 °C, which are near to the 800 °C synthesis temperature, showed similar Raman spectrum change (fig. S6 (a) and (b)). The new Raman peak at 1850 cm^{-1} appears at the same position and in the same potential range E< 0.05 V for both the samples. The presence of this reversible Raman peak in N-rGO samples only at a lower potential region indicates the possibility of formation of an intermediate species by the interaction between Li^+ electrolyte ion and N-vacancies.

Ma *et al.* have also observed a new reversible Raman peak at ~1850 cm^{-1} during charging of InN thin film electrode in 1 M bis(trifluoromethane)sulfonamide lithium (LiTFSI) electrolyte.[52] The Raman peak was associated with the formation of Li_3N species, which started to appear at the final stage of charging (low potential region) and disappeared during discharging (high potential region). Such reversible intermediate (Li_xN) formation is also possible in N-rGO samples by the intercalation of Li^+ and succeeding interaction with N-vacancies in the low potential region. It is also interesting to mention here that this type of Raman peak was only observed during the cycling of N-rGO electrodes and was not found in the case of graphite and rGO, again highlighting the role of N-vacancies. A schematic representation of the charge storage mechanism and the role of N-vacancies is shown in fig. 7. The presence of this peak in all three different types of N-rGO electrodes also eliminates the possibility of an artifact. Although the Raman peak at 1850 cm^{-1} was absent in the case N-rGO synthesized at 600 °C (fig S7), it could be due to the fact that the formation of Li_xN requires active interaction between N-vacancies and Li-ions. The incomplete reduction of GO, presence of a large number of oxygen functionalities, a lower degree of reduction, and incomplete doping of N in rGO at 600 °C can inhibit the intercalation of Li^+ into N-rGO (600 °C) sheets and thus can lead to the absence of Li_xN species formation.

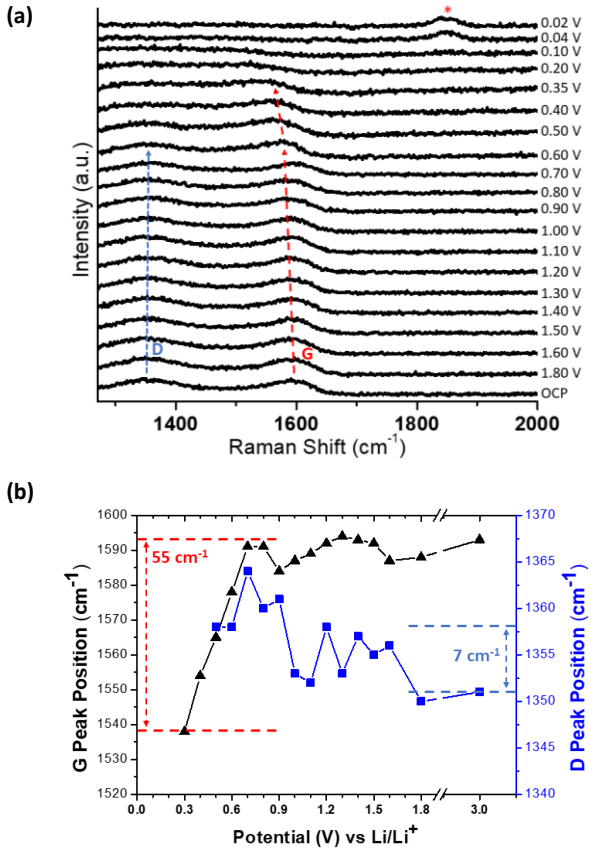

Fig. 6 (a) *In situ* EC Raman spectra of Li^+ intercalation and (b) change in Raman peak G and D of N rGO electrode (* new Raman peak observed at 1850 cm^{-1})

The role of Li_xN intermediate formation on the enhanced capacity of N-rGO (shown in fig. S4) is yet to be explored.

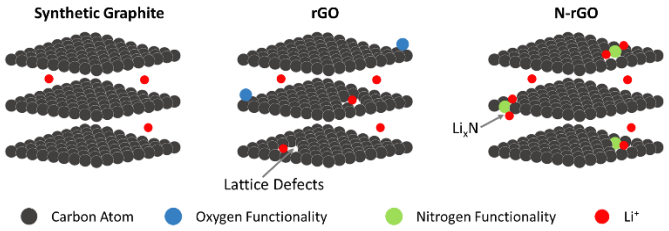

Fig. 7 Schematics of Li^+ intercalation in synthetic graphite, rGO and N-rGO.

Although based on the reported literature by Zhu *et al.* and Park *et al.*, it is depicted that lithium nitride species such as Li_3N retain high Li^+ conductivity (10^{-3} S cm^{-1}) and provide stability to the electrode over dendrite formation,[53,54] leading to the high cyclic stability. To investigate the role of Li_xN on the cyclic stability, 100 cycles of charge-discharge for N-rGO and rGO was carried out at C/2 rate and is discussed in ESI fig.S8.

Conclusion

In this work, *in situ* electrochemical Raman spectroscopy was employed to investigate lithium-ion intercalation/de-intercalation mechanisms in synthetic graphite, rGO, and N-rGO. Staged GIC formation in graphite was observed from the splitting of Raman G peak and the induced strain in the lattice was indicated by the variation in the 2D peak. For rGO and N-rGO, intercalation did not follow the staging mechanism as in graphite because of their defective structure. However, these defects help in an early and large accumulation of Li^+, observed from the red-shift in the G peak (ΔG_{rGO}= 36 cm^{-1} and $\Delta G_{N\text{-}rGO}$= 55 cm^{-1}) and early disappearance of Raman peaks. The large accumulation of Li^+ in N-rGO is due to its nitrogen vacancies and nitrogen induced defects, indicated by the larger red-shift in G peak and blue-shift in the D peak (ΔD= 7 cm^{-1}). It was also observed that interaction between Li^+ and nitrogen functionalities result in the formation of a reversible intermediate species Li_xN, identified as a new Raman peak at 1850 cm^{-1}. The presence of a new Raman peak was confirmed in other N-rGO samples with variable nitrogen doping and functionalities. This study gives an insight into the charge storage mechanism in high-performance electrode materials like rGO and N-rGO, which otherwise remain unexplored. Although, more chemical composition-based *in situ* studies are required to understand the exact intermediate species formation in the case of heteroatom doped graphene such as N-rGO.

Author Contributions

RY planned, carried out, and drafted the manuscript. PJ helped with TEM and with RY discussed the outcome of the research. MH and MY supervised and guided during research work.

Conflicts of interest

There are no conflicts to declare.

Acknowledgements

This work was supported by the Research Center for Smart Energy Technologies and Research Center for Smart Photons and Materials, Toyota Technological Institute and partially supported by the research fellowship of the Iwatani Naoji Foundation.

References

1 S. Liu, J. Xie, H. Li, Y. Wang, H. Y. Yang, T. Zhu, S. Zhang, G. Cao and X. Zhao, *J. Mater. Chem. A*, 2014, **2**, 18125, DOI:10.1039/c4ta03192j.

2 R. Yadav, P. Joshi, M. Hara, T. Yana, S. Hashimoto and M. Yoshimura, *SN Appl. Sci.*, 2020, **2**, 1630, DOI:10.1007/s42452-020-03401-x.

3 P. Joshi, H. H. Huang, R. Yadav, M. Hara and M. Yoshimura, *Catal. Sci. Technol.*, 2020, **10**, 6599.

4 M. Hara, P. Joshi, H.-H. Huang and M. Yoshimura, *ECS Meet. Abstr.*, 2020, MA2020-01(37), 1545, DOI:10.1149/ma2020-01371545mtgabs.

5 S. Xiao, H. Zhu, L. Wang, L. Chen and H. Liang, *Phys. Chem. Chem. Phys.*, 2014, **16**, 16003 , DOI:10.1039/c4cp01990c.

6 Z. Wang, S. Li, Y. Zhang and H. Xu, *Phys. Chem. Chem. Phys.*, 2018, **20**, 7447, DOI:10.1039/c7cp07960e.

7 J. Li and J. Gong, *Energy Environ. Sci.*, 2020, **13**, 3748, DOI:10.1039/d0ee01706j.

8 J. Tan, D. Liu, X. Xu and L. Mai, *Nanoscale*, 2017, **9**, 19001.

9 A. M. Tripathi, W. N. Su and B. J. Hwang, *Chem. Soc. Rev.*, 2018, **47**, 736.

10 J. He, W. Lv, Y. Chen, J. Xiong, K. Wen, C. Xu, W. Zhang, Y. Li, W. Qin and W. He, *J. Power Sources*, 2017, **363**, 103.

11 A. C. Ferrari, *Solid State Commun.*, 2007, **143**, 47, DOI:10.1016/j.ssc.2007.03.052.

12 L. M. Malard, M. A. Pimenta, G. Dresselhaus and M. S. Dresselhaus, *Phys. Rep.*, 2009, **473**, 51.

13 M. Inaba, H. Yoshida, Z. Ogumi, T. Abe, Y. Mizutani and M. Asano, *J. Electrochem. Soc.*, 1995, **142**, 20, DOI:10.1149/1.2043869.

14 L. J. Hardwick, M. Hahn, P. Ruch, M. Holzapfel, W. Scheifele, H. Buqa, F. Krumeich, P. Novák and R. Kötz, *Electrochim. Acta*, 2006, **52**, 675, DOI:10.1016/j.electacta.2006.05.053.

15 L. J. Hardwick, P. W. Ruch, M. Hahn, W. Scheifele, R. Kötz and P. Novák, *J. Phys. Chem. Solids*, 2008, **69**, 1232, DOI:10.1016/j.jpcs.2007.10.017.

16 K. Share, A. P. Cohn, R. E. Carter and C. L. Pint, *Nanoscale*, 2016, **8**, 16435, DOI:10.1039/c6nr04084e.

17 F. Bonhomme, J. C. Lassègues and L. Servant, *J. Electrochem. Soc.*, 2001, **148**, E450, DOI:10.1149/1.1409546.

18 P. Joshi, R. Yadav, M. Hara, T. Inoue, Y. Motoyama and M. Yoshimura, *J. Mater. Chem. A*, 2021, Advance Article.

19 W. Tang, B. M. Goh, M. Y. Hu, C. Wan, B. Tian, X. Deng, C. Peng, M. Lin, J. Z. Hu and K. P. Loh, *J. Phys. Chem. C*, 2016, **120**, 2600, DOI:10.1021/acs.jpcc.5b12551.

20 C. He, J. J. Zhang and P. K. Shen, *J. Mater. Chem. A*, 2013, **1**,

14586 , DOI:10.1039/c3ta14070a.
21 Z. Xing, Z. Ju, Y. Zhao, J. Wan, Y. Zhu, Y. Qiang and Y. Qian, *Sci. Rep.*, 2016, **6**, 26146, DOI:10.1038/srep26146.
22 R. Badam, P. Joshi, R. Vedarajan, R. Natarajan and N. Matsumi, *Nanoscale Res. Lett.*, 2017, **12**, 555, DOI:10.1186/s11671-017-2322-3.
23 J. He, A. Bhargav, H. Yaghoobnejad Asl, Y. Chen and A. Manthiram, *Adv. Energy Mater.*, 2020, **10**, 2001017.
24 C. Sole, N. E. Drewett and L. J. Hardwick, *Faraday Discuss.*, 2014, **172**, 223, DOI:10.1039/c4fd00079j.
25 J. Zou, C. Sole, N. E. Drewett, M. Velický and L. J. Hardwick, *J. Phys. Chem. Lett.*, 2016, **4**, 4291, DOI:10.1021/acs.jpclett.6b01886.
26 H. H. Huang, K. K. H. De Silva, G. R. A. Kumara and M. Yoshimura, *Sci. Rep.*, 2018, **8**, 6849, DOI:10.1038/s41598-018-25194-1.
27 L. K. Putri, B. J. Ng, W. J. Ong, H. W. Lee, W. S. Chang and S. P. Chai, *ACS Appl. Mater. Interfaces*, 2017, **9**, 4558, DOI:10.1021/acsami.6b12060.
28 G. Calcagno, M. Agostini, S. Xiong, A. Matic, A. E. C. Palmqvist and C. Cavallo, *Energies*, 2020, **13**, 4998, DOI:10.3390/en13194998.
29 R. Czerw, M. Terrones, J.-C. Charlier, X. Blase, B. Foley, R. Kamalakaran, N. Grobert, H. Terrones, D. Tekleab, P. M. Ajayan, W. Blau, M. Rühle and D. L. Carroll, *Nano Lett.*, 2001, **1**, 457–460.
30 C. Ma, X. Shao and D. Cao, *J. Mater. Chem.*, 2012, **22**, 8911, DOI:10.1039/c2jm00166g.
31 X. K. Kong and Q. W. Chen, *Phys. Chem. Chem. Phys.*, 2013, **15**, 12982, DOI:10.1039/c3cp51987b
32 B. Yu, D. Yang, Y. Hu, J. He, Y. Chen and W. He, *Small Methods*, 2019, **3**, 1800287.
33 Z. Lin, G. Waller, Y. Liu, M. Liu and C. P. Wong, *Adv. Energy Mater.*, 2012, **2**, 884, DOI:10.1002/aenm.201200038.
34 G. Wang, X. Shen, J. Yao and J. Park, *Carbon N. Y.*, 2009, **47**, 2049, DOI:10.1016/j.carbon.2009.03.053.
35 P. Joshi, K. Iwai, S. G. Patnaik, R. Vedarajan and N. Matsumi, *J. Electrochem. Soc.*, 2018, **165**, A493, DOI:10.1149/2.0141803jes.
36 K. H. Seng, G. D. Du, L. Li, Z. X. Chen, H. K. Liu and Z. P. Guo, *J. Mater. Chem.*, 2012, **22**, 16072, DOI:10.1039/c2jm32822d.
37 F. Xia, X. Hu, Y. Sun, W. Luo and Y. Huang, *Nanoscale*, 2012, **4**, 4707, DOI:10.1039/c2nr30742a.
38 S. L. Chou, Y. Pan, J. Z. Wang, H. K. Liu and S. X. Dou, *Phys. Chem. Chem. Phys.*, 2014, **16**, 20347, DOI:10.1039/c4cp02475c.
39 J. S. Okasinski, I. A. Shkrob, A. Chuang, M. T. F. Rodrigues, A. Raj, D. W. Dees and D. P. Abraham, *Phys. Chem. Chem. Phys.*, 2020, **22**, 21977, DOI:10.1039/d0cp04436a.
40 H. Y. Song, T. Fukutsuka, K. Miyazaki and T. Abe, *Phys. Chem. Chem. Phys.*, 2016, **18**, 27486, DOI:10.1039/c6cp05489g.
41 M. S. Dresselhaus and G. Dresselhaus, *Adv. Phys.*, 1981, **30**, 139–326.
42 J. C. Chacón-Torres, L. Wirtz and T. Pichler, *ACS Nano*, 2013, **7**, 9249, DOI:10.1021/nn403885k.
43 D. Allart, M. Montaru and H. Gualous, *J. Electrochem. Soc.*, 2018, **165**, A380–A387.
44 T. M. G. Mohiuddin, A. Lombardo, R. R. Nair, A. Bonetti, G. Savini, R. Jalil, N. Bonini, D. M. Basko, C. Galiotis, N. Marzari, K. S. Novoselov, A. K. Geim and A. C. Ferrari, *Phys. Rev. B - Condens. Matter Mater. Phys.*, 2009, **79**, 205433, DOI:10.1103/PhysRevB.79.205433.
45 K. Share, A. P. Cohn, R. Carter, B. Rogers and C. L. Pint, *ACS Nano*, 2016, **10**, 9738, DOI:10.1021/acsnano.6b05998.
46 C. T. Chan, K. M. Ho and W. A. Kamitakahara, *Phys. Rev. B*, 1987, **36**, 3499, DOI:10.1103/PhysRevB.36.3499.
47 M. Kertész, F. Vonderviszt and S. Pekker, *Chem. Phys. Lett.*, 1982, **90**, 430, DOI:10.1016/0009-2614(82)80249-2.
48 M. Kertesz, *Mol. Cryst. Liq. Cryst.*, 1985, **126:1**, 103, DOI:10.1080/15421408508084159.
49 M. Endo, C. Kim, T. Karaki, T. Fujino, M. J. Matthews, S. D. M. Brown and M. S. Dresslhaus, *Synth. Met.*, 1998, **98**, 17, DOI:10.1016/S0379-6779(98)00141-6.
50 Z. Wang, X. Huang, R. Xue and L. Chen, *Carbon N. Y.*, 1999, **37**, 685, DOI:10.1016/S0008-6223(98)00245-0.
51 M. Inaba, H. Yoshida and Z. Ogumi, *J. Electrochem. Soc.*, 1996, **134**, 2572, DOI:10.1149/1.1837049.
52 Y. Ma, L. Li, L. Wang, J. Qian, X. Hu, W. Qu, Z. Wang, R. Luo, S. Fu, F. Wu and R. Chen, *ACS Appl. Mater. Interfaces*, 2020, **12**, 31411, DOI:10.1021/acsami.0c06546.
53 K. Park, B. C. Yu and J. B. Goodenough, *Adv. Energy Mater.*, 2016, **6**, 1502534, DOI:10.1002/aenm.201502534.
54 Y. Zhu, X. He and Y. Mo, *Adv. Sci.*, 2017, **4**, 1600517, DOI:10.1002/advs.201600517.